Supplement of Atmos. Chem. Phys., 22, 6309–6325, 2022
https://doi.org/10.5194/acp-22-6309-2022-supplement

Atmospheric Chemistry and Physics
Open Access

Supplement of

Oceanic emissions of dimethyl sulfide and methanethiol and their contribution to sulfur dioxide production in the marine atmosphere

Gordon A. Novak et al.

Correspondence to: Timothy H. Bertram (timothy.bertram@wisc.edu)

S1 Lag time determination

The EC flux calculation involves the instantaneous covariance of vertical wind speed (*w'*) and the scalar of interest (*x'*) which is complicated if there are time lags between the two data sources. Lag times between measurements of *w* and *x* were determined by analysis of the cross-covariance of *w'* and *x'* data. Typically, a time lag between *x'* and *w'* would exist due to the transit time of ambient air through the inlet volume, with expected inlet gas evacuation time of approximately 1.7 s in this experiment. In addition, the internal clocks of the computers logging data from the Vocus and the sonic anemometer were not perfectly synchronized during part of the campaign, resulting in observed lag time between *w'* and DMS' or MeSH' being larger than the physical gas evacuation time of the inlet. The inlet system was rigorously leak checked and flows were recorded continuously, which confirmed that residence time in the inlet was short and constant throughout the campaign. Instrument response times to zero and calibration additions were also consistent with the calculated volumetric residence time of 1.7 s. The high frequency flux attenuation described in S4 is also not consistent with a physical inlet residence time of >10 s. These lines of evidence further support that the long cross-covariance lag times are due to poor clock synchronization and not physical transit times of the sample through the inlet. A step-change in the lag time of the cross-covariance maximum was observed corresponding to an instrument shutdown period during a planned power outage. Lag times before the instrument shutdown were on the order of 15 s and after the shutdown were on the order 32 s as shown in **Figure S1**. No abrupt changes in lag time determined during continuous sampling periods were observed. All other flux diagnostics were consistent between the periods, suggesting the change in lag time was due to clock differences between the data recording devices during the power outage and not a change in the flow rate through the sampling inlet. DMS and MeSH showed consistent strong cross-covariance peaks which enabled clear determination of the optimum lag time for all flux analysis periods. For each 30-minute flux averaging period, the optimum lag time for both DMS and MeSH were individually determined. The mean of the lag time from DMS and MeSH was then calculated and applied as the lag time for the final flux calculation from that data period.

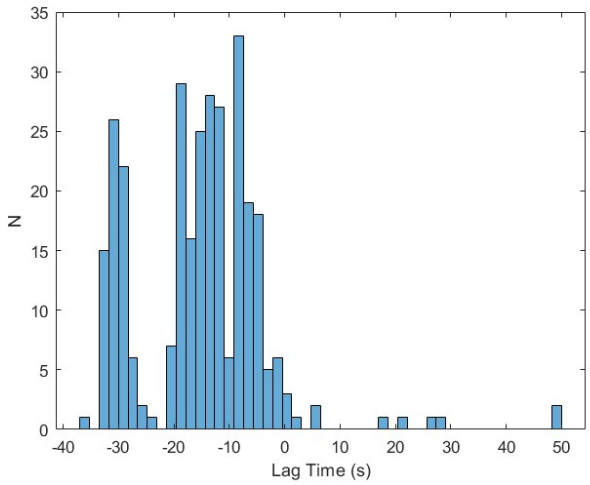

Figure S1. Histogram of optimized lag times during the campaign. The bimodal distribution corresponds to periods before and after a power outage which resulted in further desynchronization of the clocks for the data recorders.

S2 Flux LOD determination

The error in each flux averaging period (LOD) for each ion was be determined by analysis of the root mean squared error (RMSE) of the cross-covariance between vertical wind speed and mass spectrometer signal at lag times significantly longer than the calculated true lag time (Langford et al., 2015; Spirig et al., 2005; Wienhold et al., 1995). The random flux error is determined using lag windows of -150 to -180 and 150 to 180 s, which are significantly larger than the determined optimum lag times discussed in **Section S1** of 15-40 s. The selection of the -150 to -180 and 150 to 180 s lag windows is somewhat arbitrary and may still capture organized atmospheric structure that persists over long time periods. Determination of LOD by the RMSE (LOD_{RMSE}) captures variance in the cross-covariance at long lag times but also accounts for long term offsets from zero in the cross-covariance, providing a more conservative determination of the LOD compared to simply determining the standard deviation (Langford et al., 2015). The final flux LOD_{RMSE} was determined for each ion during each flux averaging period by multiplying the LOD_{RMSE} error by 3 to give the flux LOD at the 3σ confidence level. The campaign mean 3σ confidence level LOD_{RMSE} for DMS and MeSH were 0.35 and 0.11 ppt m s^{-1} respectively. 87 and 72% of individual 30-minute flux determinations were above the campaign mean 3σ LOD_{RMSE} for DMS and MeSH respectively.

S3 Flux spectral analysis and corrections

Spectral analysis provides a means to evaluate experimental performance in capturing low- and high-frequency flux signals. Here we describe the flux spectra for DMS and sensible heat (SH). Analysis of the observed frequency weighted cospectra shape of DMS and SH is useful to validate that the observed signal was not significantly attenuated at low or high frequencies. SH flux is calculated using air temperature measured directly by the sonic anemometer and should have no flux attenuation. Cospectral averaging is performed by binning frequency into 50 evenly log spaced bins and normalizing the integrated cospectra to 1. The area under the unnormalized cospectra curve is the equivalent to the flux for that observation period. Cospectra of DMS and SH from an individual flux averaging period of windspeed 4.3 m s^{-1} is shown in **Figure S2a**. The shift of the DMS cospectral curve relative to the SH curve at high frequencies (>0.1 Hz) is indicative of high frequency attenuation during sampling of DMS. Ogives of DMS, and SH from the same flux period are shown in **Figure S2b**. The ogive is the normalized cumulative distribution of the cospectra, which is used to validate both that no high-frequency attenuation is present and that the flux averaging time is sufficiently long that all frequencies contributing for the flux is captured. The apparent plateau in the ogive at low frequencies for DMS and SH validates that the selected 30-minute flux averaging time is sufficiently long to capture the largest eddies contributing to the flux. The ogive of DMS shows a generally similar spectral shape compared to the SH ogive, especially at frequencies below 0.1 Hz. At frequencies above 0.1 Hz the ogive of DMS is flatter than SH,

indicative of attenuation at these high frequencies. High pumping rates in sampling line were used to ensure that turbulent flow was always maintained in the sampling line, which reduces the effects of high frequency attenuation (Massman, 1991).

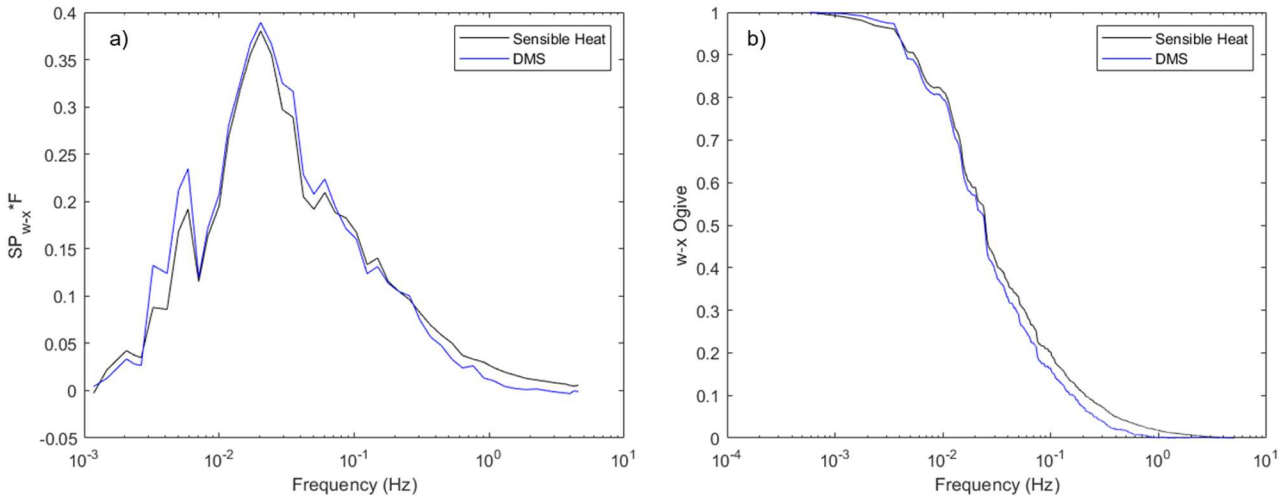

Figure S2. Example (a) cospectra and (b) ogives of DMS and sensible heat.

S4 Flux high frequency attenuation corrections

The high frequency attenuation of species measured by the Vocus was quantified and corrected for by comparison of the MeSH or DMS cospectra and the cospectra of temperature as measured by the sonic anemometer, which does not experience high frequency loss due to sampling through an inlet line. The high frequency attenuation of scalars sampled by the Vocus through the inlet line can be expressed as a low-pass filter function (Eq S1) where τ_c denotes the response time.

$$H(f) = [1 + (2\pi f \tau_c)^2]^{-1} \quad \text{(ES1)}$$

If the response time is known, the unattenuated flux magnitude can be recovered from the cospectra by applying Equation S2.

$$F_x = \int_0^{fn} C_{wxm}(f)/[H_f]^{1/2} df \quad \text{(ES2)}$$

The response time can be determined empirically by taking the ratio of the attenuated scalar normalized cospectra and the unattenuated sonic anemometer temperature normalized cospectra (Equation S3). The response time is calculated as the frequency where the attenuated signal is reduced by $1/\sqrt{2}$.

$$Cospectral\ ratio = \frac{C_{wx}(f)/F_x}{C_{wT}(f)/F_T} \quad \text{(ES3)}$$

For both MeSH and DMS τ_c was determined to be 0.5 ± 0.1 s. Correction factors for MeSH and DMS flux were determined following the method outlined by Bariteau et al., (2010) where 1.) The parametrized cospectra from Kaimal et al., (1972) is calculated using Equation S4. Where $n=fz/U$, z is the inlet height, and U is the mean wind speed. 2.) The low-pass filter function (ES1) with the determined instrument response time is applied to the Kaimal cospectra (Equation S5). 3.) The flux

attenuation correction multiplication factor ($Corr\_f$) is calculated by taking the ratio of the integrated flux from the attenuated (F_{xm_K}) and un-attenuated (F_{x_K}) Kaimal cospectrum (Equation S6).

$$\frac{fC_{wx_K}(f)}{F_x} = \frac{11n}{(1+13.3n)^{7/4}} \quad \text{(ES4)}$$

$$F_{xm\_K} = \int_0^{fn} C_{wx_K}(f)[H(f)]^{1/2}df \quad \text{(ES5)}$$

$$Corr\_f = \frac{F_{xm\_K}}{F_{x\_K}} \quad \text{(ES6)}$$

Resulting calculated flux attenuation correction factors were on the order of 8%. This correction factor was applied to the measured EC flux of DMS and MeSH for all flux values reported in this work.

The empirical model of Horst, (1997) shown in Equation. S7 provides an alternative method to estimate and correct for high frequency flux attenuation. For our determined instrument response time (τ_c) for DMS of 0.5 s and a wind speed of 2.9 m s^{-1} (the campaign daytime mean) we calculate the flux attenuation to be on the order of 8%, in good agreement with the explicit low pass filter function correction method described above.

$$\frac{F_m}{F_x} = \frac{1}{1+(2\pi n_m \tau_c U/z)^{\alpha}} \quad \text{(ES7)}$$

Where F_m/F_x is the ratio of the measured flux to the unattenuated flux, U is wind speed, z is measurement height, and n_m and α are scaling factors for an unstable boundary layer taken as 0.085 and 7/8 respectively.

S5 HPMTF chemistry implementation

The formation of hydroperoxymethyl thioformate (HPMTF; $HOOCH_2SCHO$) from DMS oxidation was also added to the model oxidative mechanism. HPMTF has recently been observed to be a major stable DMS oxidation product in global airborne observations (Veres et al., 2020). DMS oxidation through the hydrogen abstraction pathway, yields the short-lived methylthiomethylperoxy radical (MTMP; CH_3SCH_2OO), which in the relatively pristine MBL, undergoes efficient unimolecular isomerization to HPMTF, outpacing bimolecular chemistry. We set the MTMP autoxidation rate that produces HPMTF as the temperature dependent first H-shift as presented in Veres et al. (2020) ($k_{H\text{-}shift}$ = 0.041 s^{-1} at 293 K, $k_{H\text{-}shift}$ (T) = (2.2433 × 10^{11}) × exp(-9.8016 × 10^3/T) × exp(1.0348 × 10^8/(T^3))). The bimolecular rate constant of HPMTF with OH ($k_{OH+HPMTF}$) was approximated to be 1.1 × 10^{-11} × 10^{-11} molecules cm^{-3} s^{-1} which is the rate of OH + methyl thioformate which is structurally similar molecule to HPMTF, which is within the uncertainty range of a recent laboratory determination of 1.4 (0.27 – 2.4 uncertainty range) x 10^{-11} cm^3 molec^{-1} s^{-1} (Jernigan et al., 2022). The reaction of HPMTF + OH is assumed to produce SO_2 at unit yield based upon preliminary laboratory studies. Uptake of HPMTF and other reactive trace gases to marine aerosol particles is treated as heterogenous loss with a unimolecular rate constant (k_{het}) calculated from Equation S8.

$$k_{het} = \frac{\gamma A \bar{c}}{4} \quad \text{(ES8)}$$

where γ is the dimensionless uptake coefficient, A is the particle surface area density (μm^2 cm^{-3}), and $\bar{c}$ is the mean molecular speed of the molecule of interest (cm s^{-1}). A constant particle surface area of 150 μm^2 cm^{-3} is used, based on published

observations of typical coastal, marine aerosol particle size distributions (Collins et al., 2013; Modini et al., 2015; Ryder et al., 2014). γ_{HPMTF} when included in the model was taken as 0.01.

HPMTF heterogeneous loss terms to aerosol particles and clouds and dry deposition to the ocean surface serve to reduce the effective SO_2 yield from DMS as these terms act as terminal volatile sulfur sinks. In the default model implementation described previously only HPMTF surface deposition was included. Inclusion of HPMTF heterogeneous chemistry with aerosol particles reduces model net SO_2 production from DMS to 2.7 ppt h^{-1} compared to 5.8 ppt h^{-1} in a model case without HPMTF chemistry ($k_{H\text{-}Shift}$ = 0 s^{-1}), taking F_{DMS} at the campaign mean of 1.13 ppt m s^{-1}. The model implementation of HPMTF loss terms in this work uses a simplified approach of a clear-sky conditions (no cloud loss), constant aerosol surface area (150 um^2 cm^{-3}), constant reactive uptake coefficient (γ = 0.01), and a constant deposition velocity (v_{ex} = 0.78 cm s^{-1} from Vermeuel et al. (2020)) which do not capture the variability of the global marine boundary layer. Uptake of HPMTF to cloud droplets has been proposed to be a significant loss term for HPMTF in the cloudy marine boundary layer, which would further reduce SO_2 production compared to the case presented here (Novak et al., 2021; Veres et al., 2020; Vermeuel et al., 2020). HPMTF cloud loss was not considered in any of the model cases presented in this work.

Table S1. Updated F0AM oxidation mechanisms for DMS (CH_3SCH_3), MeSH (CH_3SH), and HPMTF ($HOOCH_2SCHO$) chemistry. Only newly added reactions and the key reactions leading to SO_2 formation from MeSH are detailed here.

REVISED DMS/HPMTF MECHANISM	RATE	INCLUDED IN BASE MCM V3.3.1	CITATION
$CH_3SH + OH \rightarrow CH_3S$	$k(T) = (9.9 \times 10^{-12}) \times \exp(360/T)$	N	1,2
$CH_3SH + BrO \rightarrow CH_3S$	$k(T) = (2.2 \times 10^{-15}) \times \exp(830/T)$	N	3
$CH_3SH + NO_3 \rightarrow CH_3S$	$k = 9.2 \times 10^{-13}$	N	4
$CH_3S + NO_2 \rightarrow CH_3SO + NO$	$k(T) = (6 \times 10^{-11}) \times \exp(240/T)$	Y	
$CH_3S + O_3 \rightarrow CH_3SO$	$k(T) = (1.15 \times 10^{-12}) \times \exp(430/T)$	Y	
$CH_3S \rightarrow CH_3SOO$	$k(T) = (1.2 \times 10^{-16}) \times \exp(1580/T) \times [O_2]$	Y	
$CH_3SO \rightarrow CH_3S(O)OO$	$k(T) = (3.12 \times 10^{-16}) \times \exp(1580/T) \times [O_2]$	Y	
$CH_3SO + O_3 \rightarrow CH_3O_2 + SO_2$	$k = 4.0 \times 10^{-11}$	Y	
$CH_3SO + NO_2 \rightarrow$ $0.75(CH_3S(O)O + NO)$ $0.25(CH_3O_2 + SO_2 + NO)$	$k = 1.2 \times 10^{-11}$	Y	
$CH_3SOO + NO \rightarrow NO_2 + CH_3SO$	$k = 1.1 \times 10^{-11}$	Y	
$CH_3SOO + NO_2 \rightarrow NO3 + CH_3SO$	$k = 2.2 \times 10^{-11}$	Y	
$CH_3SOO \rightarrow CH_3O_2 + SO_2$	$k(T) = (5.6 \times 10^{16}) \times \exp(-10870/T)$	Y	
$CH_3SOO \rightarrow CH_3S$	$k(T) = (3.5 \times 10^{10}) \times \exp(-3560/T)$	Y	
$CH_3S(O)O + O_3 \rightarrow CH_3SO_3$	$k = 3.0 \times 10^{-13}$	Y	
$CH_3SO_3 + HO_2 \rightarrow MSA + O_3$	$k = 5.0 \times 10^{-11}$	Y	
$CH_3SO_3 \rightarrow CH_3O_2 + SO_3$	$k(T) = (5.0 \times 10^{13}) \times \exp(-9946/T)$	Y	
$CH_3S(O)O + O_3 \rightarrow CH_3O_2 + SO_2$	$k(T) = (5.0 \times 10^{13}) \times \exp(-9673/T)$	Y	
$CH_3SCH_3 + OH \rightarrow HODMSO_2$	$k(T, O2) = (9.5E\text{-}39 \times [O2] \times \exp(5270/T)) / (1 + 7.5E\text{-}29 \times [O_2] \times \exp(5610/T) \times 0.2095)$	Y	
$CH_3SCH_3 + OH \rightarrow CH_3SCH_2O_2 + H_2O$	$k(T) = (1.12 \times 10^{-11}) \times \exp(-250/T)$	Y	
$CH_3SCH_3 + Cl \rightarrow CH_3SCH_2O_2 + HCl$	$k(T) = (9.4 \times 10^{-11}) \times \exp(190/T)$	N	4
$CH_3SCH_3 + NO_3 \rightarrow CH_3SCH_2O_2 + HNO_3$	$k(T) = (1.9 \times 10^{-13}) \times \exp(520/T)$	Y	
$CH_3SCH_3 + BrO \rightarrow MSA + products$	$k = (1.4 \times 10^{-14}) \times \exp(950/T)$	N	4
$CH_3SCH_2O_2 + HO_2 \rightarrow SO_2 + products$	$k(T) = (1.13 \times 10^{-13}) \times \exp(1300/T)$	Y	
$CH_3SCH_2O_2 + RO_2 \rightarrow SO_2 + products$	$k = 1.0 \times 10^{-11}$ cm^3 molec.$^{-1}$ s^{-1}	Y	
$CH_3SCH_2O_2 + NO \rightarrow SO_2 + products$	$k = (4.9 \times 10^{-12}) \times \exp(260/T)$	Y	
$CH_3SCH_2O_2 + NO_3 \rightarrow SO_2 + products$	$k = 2 \times 10^{-12}$ cm^3 molec.$^{-1}$ s^{-1}	Y	
$CH_3SCH_2O_2 \rightarrow HPMTF$	$k_{calc}(T) = (2.2433 \times 10^{11}) \times \exp(-9.8016 \times 10^3/T) \times \exp(1.0348 \times 10^8/(T^3))$	N	5

$\mathbf{HPMTF + OH \rightarrow SO_2 + products}$	$k = 1.11 \times 10^{-11}$ cm^3 molec.$^{-1}$ s^{-1}	N	6,7
$\mathbf{HPMTF + aerosol \rightarrow SO_4^{2-} + products}$	$\gamma = 0.01$	N	8

1. Tyndall and Ravishankara, 1989
2. Butkovskaya and Setser, 2021
3. Aranda et al., 2002, note experiments were at low pressure and extrapolation to ambient pressure is uncertain.
4. Burkholder et al., 2020
5. Veres et al., 2020
6. Patroescu et al., 1996
7. Vermeuel et al., 2020
8. Assumed value

Table S2. Fixed chemical inputs in the F0AM MCM box model.

MOLECULE	CONCENTRATION (PPB)
H_2	522
CH_4	1878
CO	94
H_2O_2	0.35
HNO_3	0.1
NO_X ($NO + NO_2$)	0.25
C_5H_8 (ISOPRENE)	0.1

References

Aranda, A., Díaz De Mera, Y., Rodríguez, D., Salgado, S. and Martínez, E.: Kinetic and products of the BrO+CH3SH reaction: Temperature and pressure dependence, Chem. Phys. Lett., 357(5–6), 471–476, doi:10.1016/S0009-2614(02)00561-4, 2002.

Bariteau, L., Helmig, D., Fairall, C. W., Hare, J. E., Hueber, J. and Lang, E. K.: Determination of oceanic ozone deposition by ship-borne eddy covariance flux measurements, Atmos. Meas. Tech., 3(2), 441–455, doi:10.5194/amt-3-441-2010, 2010.

Burkholder, J. B., Sander, S. P., Friedl, R. R., Golden, D. M., Kurylo, M. J., Moortgat, G. K., Wine, P. H., Ravishankara, a R., Kolb, C. E., Molina, M. J., Diego, S., Jolla, L., Huie, R. E. and Orkin, V. L.: Chemical Kinetics and Photochemical Data for Use in Atmospheric Studies Evaluation Number 15, , 19 [online] Available from: http://jpldataeval.jpl.nasa.gov/, 2020.

Butkovskaya, N. I. and Setser, D. W.: Reactions of OH and OD radicals with simple thiols and sulfides studied by infrared chemiluminescence of isotopic water products: Reaction OH + CH3SH revisited, Int. J. Chem. Kinet., 53(6), 702–715, doi:10.1002/kin.21475, 2021.

Collins, D. B., Ault, A. P., Moffet, R. C., Ruppel, M. J., Cuadra-Rodriguez, L. A., Guasco, T. L., Corrigan, C. E., Pedler, B. E., Azam, F., Aluwihare, L. I., Bertram, T. H., Roberts, G. C., Grassian, V. H. and Prather, K. A.: Impact of marine biogeochemistry on the chemical mixing state and cloud forming ability of nascent sea spray aerosol, J. Geophys. Res. Atmos., 118(15), 8553–8565, doi:10.1002/jgrd.50598, 2013.

Horst, T. W.: A simple formula for attenuation of eddy fluxes measured with first-order-response scalar sensors, Boundary-Layer Meteorol., 82(2), 219–233, doi:10.1023/A:1000229130034, 1997.

Jernigan, C. M., Fite, C. H., Vereecken, L., Berkelhammer, M. B., Rollins, A. W., Rickly, P. S., Novelli, A., Taraborrelli, D., Holmes, C. D. and Bertram, T. H.: Efficient Production of Carbonyl Sulfide in the Low-NO x Oxidation of Dimethyl Sulfide , Geophys. Res. Lett., 49(3), 1–11, doi:10.1029/2021gl096838, 2022.

Kaimal, J. C., Wyngaard, J. C., Izumi, Y. and Coté, O. R.: Spectral characteristics of surface-layer turbulence, Q. J. R. Meteorol. Soc., 98(417), 563–589, doi:10.1002/qj.49709841707, 1972.

Langford, B., Acton, W., Ammann, C., Valach, A. and Nemitz, E.: Eddy-covariance data with low signal-to-noise ratio: Time-lag determination, uncertainties and limit of detection, Atmos. Meas. Tech., 8(10), 4197–4213, doi:10.5194/amt-8-4197-2015, 2015.

Massman, W. J.: The attenuation of concentration fluctuations in turbulent flow through a tube, J. Geophys. Res. Atmos., 96(D8), 15269–15273, doi:10.1029/91JD01514, 1991.

Modini, R. L., Frossard, A. A., Ahlm, L., Russel, L. M., Corrigan, C. E., Roberts, G. C., Hawkins, L. N., Schroder, J. C., Bertram, A. K., Zhao, R., Lee, A. K. ., Abbatt, J. P. D., Lin, J., Nenes, A., Wang, Z., Wonaschutz, A., Sorooshian, A., Noone, K. J., Jonsson, H., Seinfeld, J. H., Toom-Sauntry, D., Macdonald, A. M. and Leaitch, W. R.: Primary marine aerosol-cloud interactions off the coast of California, J. Geophys. Res., 120(2006), 1751–1762, doi:10.1002/2014JD022963.Received, 2015.

Novak, G. A., Fite, C. H., Holmes, C. D., Veres, P. R., Neuman, J. A., Faloona, I., Thornton, J. A., Wolfe, G. M., Vermeuel, M. P., Jernigan, C. M., Peischl, J., Ryerson, T. B., Thompson, C. R., Bourgeois, I., Warneke, C., Gkatzelis, G. I., Coggon, M. M., Sekimoto, K., Bui, T. P., Dean-Day, J., Diskin, G. S., DiGangi, J. P., Nowak, J. B., Moore, R. H., Wiggins, E. B., Winstead, E. L., Robinson, C., Thornhill, K. L., Sanchez, K. J., Hall, S. R., Ullmann, K., Dollner, M., Weinzierl, B., Blake, D. R. and Bertram, T. H.: Rapid cloud removal of dimethyl sulfide oxidation products limits SO 2 and cloud condensation nuclei production in the marine atmosphere, Proc. Natl. Acad. Sci., 118(42), e2110472118, doi:10.1073/pnas.2110472118, 2021.

Patroescu, I. V., Barnes, I. and Becker, K. H.: FTIR kinetic and mechanistic study of the atmospheric chemistry of methyl thiolformate, J. Phys. Chem., 100(43), 17207–17217, doi:10.1021/jp961452u, 1996.

Ryder, O. S., Ault, A. P., Cahill, J. F., Guasco, T. L., Riedel, T. P., Cuadra-Rodriguez, L. A., Gaston, C. J., Fitzgerald, E., Lee, C., Prather, K. A. and Bertram, T. H.: On the role of particle inorganic mixing state in the reactive uptake of N2O5 to ambient aerosol particles, Environ. Sci. Technol., 48(3), 1618–1627, doi:10.1021/es4042622, 2014.

Spirig, C., Neftel, A., Ammann, C., Dommen, J., Grabmer, W., Thielmann, A., Schaub, A., Beauchamp, J., Wisthaler, A. and Hansel, A.: Eddy covariance flux measurements of biogenic VOCs during ECHO 2003 using proton transfer reaction mass spectrometry, Atmos. Chem. Phys., 5, 465–481, doi:10.5194/acp-5-465-2005, 2005.

Tyndall, G. S. and Ravishankara, A. R.: Kinetics of the reaction of the methylthio radical with ozone at 298 K, J. Phys. Chem., 93(12), 4707–4710, doi:10.1021/j100349a006, 1989.

Veres, P. R., Andrew Neuman, J., Bertram, T. H., Assaf, E., Wolfe, G. M., Williamson, C. J., Weinzierl, B., Tilmes, S., Thompson, C. R., Thames, A. B., Schroder, J. C., Saiz-Lopez, A., Rollins, A. W., Roberts, J. M., Price, D., Peischl, J., Nault, B. A., Møller, K. H., Miller, D. O., Meinardi, S., Li, Q., Lamarque, J.-F. F., Kupc, A., Kjaergaard, H. G., Kinnison, D., Jimenez, J. L., Jernigan, C. M., Hornbrook, R. S., Hills, A., Dollner, M., Day, D. A., Cuevas, C. A., Campuzano-Jost, P., Burkholder, J., Paul Bui, T., Brune, W. H., Brown, S. S., Brock, C. A., Bourgeois, I., Blake, D. R., Apel, E. C., Ryerson, T. B., Neuman, J. A., Bertram, T. H., Assaf, E., Wolfe, G. M., Williamson, C. J., Weinzierl, B., Tilmes, S., Thompson, C. R., Thames, A. B., Schroder, J. C., Saiz-Lopez, A., Rollins, A. W., Roberts, J. M., Price, D., Peischl, J., Nault, B. A., Møller, K. H., Miller, D. O., Meinardi, S., Li, Q., Lamarque, J.-F. F., Kupc, A., Kjaergaard, H. G., Kinnison, D., Jimenez, J. L., Jernigan, C. M., Hornbrook, R. S., Hills, A., Dollner, M., Day, D. A., Cuevas, C. A., Campuzano-Jost, P., Burkholder, J., Bui, T. P., Brune, W. H., Brown, S. S., Brock, C. A., Bourgeois, I., Blake, D. R., Apel, E. C. and Ryerson, T. B.: Global airborne sampling reveals a previously unobserved dimethyl sulfide oxidation mechanism in the marine atmosphere, Proc. Natl. Acad. Sci. U. S. A., 117(9), 4505–4510, doi:10.1073/pnas.1919344117, 2020.

Vermeuel, M. P., Novak, G. A., Jernigan, C. M. and Bertram, T. H.: Diel profile of hydroperoxymethyl thioformate: evidence for surface deposition and multiphase chemistry, Environ. Sci. Technol., 54(19), 12521–12529, doi:10.1021/acs.est.0c04323, 2020.

Wienhold, F. G., Welling, M. and Harris, G. W.: Micrometeorological measurement and source region analysis of nitrous oxide fluxes from an agricultural soil, Atmos. Environ., 29(17), 2219–2227, doi:10.1016/1352-2310(95)00165-U, 1995.